

AD-A181 468

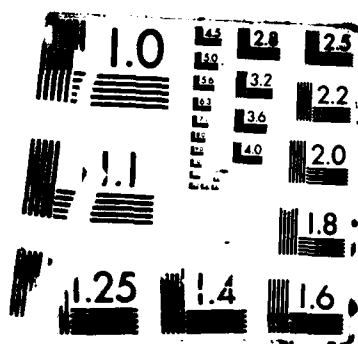
MICROWAVE SPECTROSCOPY OF A SOLAR ACTIVE REGION
OBSERVED DURING A PARTIAL ECLIPSE (U) CALIFORNIA INST OF
TECH PASADENA D E GARY ET AL. APR 76 AFGL-TR-87-0123
F19628-84-K-0023 F/C 3/2

1/1

UNCLASSIFIED

NL

END
PAGE
1/1



DTIC FILE COPY

(12)

AD-A181 468

AFGL-TR-87-0123

**MICROWAVE SPECTROSCOPY OF A SOLAR ACTIVE REGION
OBSERVED DURING A PARTIAL ECLIPSE**

D. E. Gary and G. J. Hurford

**California Institute of Technology
Pasadena, CA 91125**

April 1986

**Final Scientific Report
1 January 1984 - 31 December 1985**

**DTIC
ELECTE
JUN 19 1987
S D**

APPROVED FOR PUBLIC RELEASE; DISTRIBUTION UNLIMITED

**AIR FORCE GEOPHYSICS LABORATORY
AIR FORCE SYSTEMS COMMAND
UNITED STATES AIR FORCE
HANSCOM AIR FORCE BASE, MASSACHUSETTS 01731**

87 6 18 018

"This technical report has been reviewed and is approved for publication"

Edward W. Cliver

EDWARD CLIVER
Space Particles Environment Br
Space Physics Division

E. G. Mullen

E. G. MULLEN, Chief
Space Particles Environment Br
Space Physics Division

FOR THE COMMANDER

Rita P. Sagalyn

(Signature)
RITA SAGALYN
Division Director

This report has been reviewed by the ESD Public Affairs Office (PA) and is releasable to the National Technical Information Services (NTIS).

Qualified requestors may obtain additional copies from the Defense Technical Information Center. All others should apply to the National Technical Information Service.

If your address has changed, or if you wish to be removed from the mailing list, or if the addressee is no longer employed by your organization, please notify AFGL/DAA, Hanscom AFB, MA 01731. This will assist us in maintaining a current mailing list.

Do not return copies of this report unless contractual obligations or notices on a specified document requires that it be returned.

A181468

REPORT DOCUMENTATION PAGE		READ INSTRUCTIONS BEFORE COMPLETING FORM	
1. REPORT NUMBER AFGL-TR-87-0123		2. GOVT ACCESSION NO.	
4. TITLE (and Subtitle) Microwave Spectroscopy of a Solar Active Region Observed during a Partial Eclipse		3. RECIPIENT'S CATALOG NUMBER	
		5. TYPE OF REPORT & PERIOD COVERED Final Scientific Report 1/1/84 - 12/31/85	
7. AUTHOR(s) D. E. Gary and G. J. Hurford		6. PERFORMING ORG. REPORT NUMBER	
9. PERFORMING ORGANIZATION NAME AND ADDRESS California Institute of Technology 1201 E. California Blvd. Pasadena, CA 91125		8. CONTRACT OR GRANT NUMBER(s) F19628-84-K-0023	
11. CONTROLLING OFFICE NAME AND ADDRESS Air Force Geophysics Laboratory Hanscom AFB, Massachusetts 01731 Monitor/ Edward Cliver PHG		10. PROGRAM ELEMENT, PROJECT, TASK AREA & WORK UNIT NUMBERS 61102F 2311G3BJ	
14. MONITORING AGENCY NAME & ADDRESS (if different from Controlling Office)		12. REPORT DATE April 1986	
		13. NUMBER OF PAGES 26	
		15. SECURITY CLASS. (of this report) Unclassified	
		15a. DECLASSIFICATION/DOWNGRADING SCHEDULE	
16. DISTRIBUTION STATEMENT (of this Report) Approved for public release; distribution unlimited			
17. DISTRIBUTION STATEMENT (of the abstract entered in Block 20, if different from Report)			
18. SUPPLEMENTARY NOTES			
19. KEY WORDS (Continue on reverse side if necessary and identify by block number) VLA Analysis OVRO Analysis Coronal Plasma Microwave Spectroscopy			
20. ABSTRACT (Continue on reverse side if necessary and identify by block number) This work presents the first attempt at using microwave spectroscopy as a diagnostic tool for the study of complex solar active regions. Since the relevant emission mechanisms are gyroresonance opacity and thermal bremsstrahlung (free-free), the microwave emission is expected to depend on the values of temperature, density and magnetic fields in the solar corona.			

Unclassified

SECURITY CLASSIFICATION OF THIS PAGE (When Data Entered)

The frequency-agile interferometer of the Owens Valley Radio Observatory was used to acquire data at 16 frequencies between 1.4 and 8 GHz in both right and left circular polarization. The special circumstances afforded by the 30 May 1984 solar eclipse were exploited to provide 2.6 arcsecond spatial resolution in one dimension at each frequency. Two dimensional VLA maps at 1.4 and 4.9 GHz were also obtained to provide 2-dimensional data.

The spectral data clearly show the transition from the gyroresonance-dominated emission at high frequencies to the free-free opacity dominated regime at lower frequencies. The thermal free-free radiation at frequencies less than 3 GHz, did not occur at the site of strongest magnetic fields near the sunspots. Instead, potential field calculations, based on a photospheric magnetogram from Kitt Peak support the interpretation that the low frequency emission originated from the top of an arcade of loops stretching between sunspots.

In most locations, at frequencies above 3 GHz the emission was found to be primarily due to gyroresonance, and was located at sites of the strongest coronal magnetic fields. The spectral cutoff at 5.4 GHz above one sunspot indicated a maximum coronal field strength of 640 gauss while the main spot had a coronal field in excess of 1430 gauss, since it remained a source of gyroresonance emission above 8 GHz in both polarizations.

A marked asymmetry in the position of the sources, was noted at frequencies down to at least 1.8 GHz, suggesting that a deficit of temperature and/or density existed on the presumably open field lines in the outer part of the spots, on the side away from the active region.

The analyses suggest that spatially resolved microwave spectroscopy may provide a viable tool for determination of plasma and magnetic field conditions in the active solar corona.

Unclassified

SECURITY CLASSIFICATION OF THIS PAGE(When Data Entered)

TABLE OF CONTENTS

I. Introduction	1
II. VLA Analysis	2
III. OVRO Analysis	4
IV. The Coronal Plasma and Active Region Structure	5
A. Identification of Emission Mechanisms	5
B. Ring Structure and Cool Plumes	6
C. The 1.4 GHz Source: An Arcade of Loops	7
V. Summary	8
Acknowledgements	9
References	9
Figure Captions	12



Accession For	
NTIS CRA&I	<input checked="" type="checkbox"/>
DTIC TAB	<input type="checkbox"/>
Unannounced	<input type="checkbox"/>
Justification	
By	
Distribution/	
Availability Codes	
Dist	Avail and/or Special
A1	

MICROWAVE SPECTROSCOPY OF A SOLAR ACTIVE REGION OBSERVED DURING A PARTIAL ECLIPSE

D. E. Gary and G. J. Hurford

264-33 Caltech
Pasadena, CA 91125

I. INTRODUCTION

Microwave emission from solar active regions has been observed with high spatial resolution for many years (Kundu, Becker, and Velusamy 1974; Kundu and Alissandrakis 1975; Erskine, Kundu, and Rao 1980; Lang and Willson 1979; Kundu and Velusamy 1980; and later papers). The high-resolution observations have helped confirm earlier indications of the role of gyroresonance emission in accounting for the intense sources of microwave emission associated with sunspots (eg Alissandrakis, Kundu, and Lantos 1980). Further evidence for gyroresonance emission at 5 GHz was obtained by observations of "ring structure" (Alissandrakis and Kundu 1982) and polarized "horseshoes" (Lang and Willson 1982).

Observations at longer wavelengths, however, have shown an entirely different picture. The observation of the full disk of the Sun at 1.4 GHz by Dulk and Gary (1983) revealed large sources associated not with individual sunspots but with the entire active region complex. The resulting full Sun map is reminiscent of soft X-ray pictures. The coronal brightness over magnetic neutral lines near the centers of active regions and the low ($< 20\%$) circular polarization away from the neutral lines was found to be fully consistent with thermal bremsstrahlung (free-free) emission from electrons at coronal temperatures. Observations from Arecibo at 2.4 GHz by Lang and Willson (1983) showed great similarity to the 1.4 GHz observations of Dulk and Gary (1983). However, since free-free emission can be expected to decline in importance at higher frequencies, it remained uncertain whether gyroresonance or free-free emission was dominant.

At higher frequencies in the millimeter wavelength regime, gyroresonance opacity and free-free opacity in the corona are both unimportant, and the appearance of active regions is dominated by relatively low contrast features generated by free-free opacity in the chromosphere (Hurford 1986).

Such previous work has shown that the selection of observing frequency can dramatically influence the appearance of solar active regions. As the dominant emission mechanism changes from free-free to gyroresonance emission between the most commonly observed frequencies, 1.4

and 4.9 GHz (Lang, Willson. and Gaizauskas 1983; Shevqaonkar and Kundu 1985) the maps have virtually no common features. Soviet workers have conducted multifrequency observations of active regions between 7.5 and 15 GHz using their RATAN-600 facility (Akhmedov et al. 1986). In most cases, however, detailed modeling has not been attempted to match spatially resolved observations at more than one frequency.

The microwave spectrum nevertheless contains a wealth of information about the solar active region atmosphere. Such information can be exploited when observations at a sufficient number of closely spaced frequencies are available. Observations at up to 86 frequencies between 1 and 18 GHz are now being made routinely with the Frequency-Agile Interferometer at the Owens Valley Radio Observatory (OVRO) (Hurford, Read, and Zirin 1984). Because the small number of baselines (1 or 3) limits the complexity of the source structure which can be handled by conventional aperture synthesis techniques, the sources discussed to date have been limited to simple isolated sunspots (Hurford, Gary and Garrett 1985; Hurford 1985).

This report presents observations obtained at OVRO and at the Very Large Array (VLA) during the partial solar eclipse of 1984 May 30. The eclipse provided a moving lunar limb which progressively occulted a solar active region. This significantly enhanced the imaging capability at OVRO, where data was obtained at 16 frequencies over the spectral range 1.4 to 8 GHz. The eclipse enabled the spatial variation of the microwave brightness temperature spectrum of a complex active region to be studied for the first time.

In Section II we present the VLA observations, describe the eclipse mapping technique and present the maps obtained at 1.4 and 4.9 GHz. In Section III we describe the analysis of the OVRO data and present the derived brightness temperature spectra. In Section IV photospheric magnetogram data is combined with the radio data to provide a coherent picture of the corona above the active region. Finally, we summarize our conclusions in Section V.

II. VLA ANALYSIS

The configuration of the Sun and Moon, as seen from the VLA on 1984 May 30, is shown in Figure 1. The VLA was operating in the C configuration as two subarrays, with the inner 13 antennas of each arm of the yee-shaped array operating at 4.9 GHz (6 cm) while the outer 13 antennas in each arm were operated simultaneously at 1.4 GHz (20 cm). The angular resolution was 6.2" and 13.8" at 4.9 GHz and 1.4 GHz respectively. The field of view at 4.9 GHz, as indicated by the circle in Figure 1, encompassed Boulder Active Region 4500. The positions of the lunar limb at 1635

and 1650 UT are also indicated. The 1.4 GHz field of view was a circle roughly the angular size of the Sun, centered on the solar meridian at latitude 40 S. The data were calibrated in phase and relative amplitude by observing a calibrator source before and after the observation. The absolute amplitude calibration was done by comparison with the OVRO amplitudes, which in turn were calibrated by observing 3C84, and adopting a flux of 60 Jy at 4.9 GHz. (We have since learned (Aller et al. 1985) that our adopted value was about 4% too high.)

The eclipse observations were analyzed using an improved version of the mapping technique used on previous VLA eclipse observations (Marsh, Hurford, and Zirin, 1980). At each frequency, the 13 antennas used during the eclipse produced 78 measurements of complex visibilities of the source region each 10 s. A normal 10 s snap-shot map gives a poor representation of the source brightness distribution $B(x,y)$ because 78 u-v components are insufficient to map a source as complex as a solar active region. However, the difference of two successive visibility measurements is almost entirely due to the change of $B(x,y)$ that occurred between the measurements. In this case this difference in brightness is restricted to sources located in narrow annulus about 4 arcseconds wide. The limited spatial complexity of sources within this narrow annulus can be well-determined with only 78 u-v components.

The analysis procedure consisted of subtracting the measured visibilities for successive 10 second samples, and then applying conventional image synthesis techniques to the differenced data to form a set of images. Cleaning was restricted to the narrow annular "window" defined by the corresponding lunar limb positions. After determining the flux within each annular "window" for each 10 s differential data sample, the annular strips were combined as in a mosaic to generate the complete map of the active region.

The resulting maps are shown to the same scale in Figure 2. The crosses show the positions of the three major sunspots of the region as measured from H-alpha full disk images (such as Fig. 1) from Big Bear Solar Observatory. At 4.9 GHz each of the three spots in the active region appear as separate sources, but with a significant asymmetry in spots 1 and 3. At 1.4 GHz, no separate spot sources are visible. Rather, there is a single elongated source which spans the entire region and is displaced from the optical spot positions.

III. OVRO ANALYSIS

The eclipse geometry at OVRO as illustrated in Figure 3 shows the positions of the lunar limb at one minute intervals, overlaid on the 4.9 GHz VLA map. Interferometric amplitudes and phases were measured every 10 s at 16 frequencies in the range 1.4 to 8 GHz, in both right and left circular polarization. As with the VLA data, the OVRO data was vector differentiated so that each differenced data sample represents the flux due to sources within an annular window defined by successive positions of the lunar limb.

Because the interferometer responds only to unresolved sources, signals from the background sun are suppressed. Yet the fringe spacing was sufficiently coarse that the small scale sources are unresolved. Thus it is the moving limb that enables the sequence of differenced amplitudes to provide spatial resolution. Because the window is moving across the active region, the variation of flux with time represents the one dimensional spatial variation of flux. The resolution perpendicular to the direction of the motion of the lunar limb is 2.6 arcseconds, independent of frequency. Figure 4 shows this cross-sectional flux variation at a few representative frequencies. At low frequencies, a single large source is evident, in agreement with the 1.4 GHz VLA map of Figure 2. At higher frequencies, the bifurcation of the source into two sources becomes apparent, as in the 5 GHz VLA map of Figure 2. Since such time profiles are available at 16 frequencies, individual flux spectra can be constructed, with six independent spectra obtained within each of the narrow annuli shown in Figure 3.

To convert these flux density spectra into brightness temperature spectra, the distribution of flux along the window must be known. In the present case, we make the assumptions that (i) the extension of the source along the window at each frequency is the same as the measured extent perpendicular to the window (as indicated by the width of the sources in the time profiles of Figure 4), and that (ii) only a single source dominates along the window at any time. The validity of these assumptions may be checked at 5 GHz by referring to Figure 3. Here it is evident that the main spots are roughly of the same extent along the window as across it. The assumption that only one source lies along the window is violated for the main spot near 1619 UT, since the second spot also lies along the window. However, the main spot so dominates the flux, at least near 5 GHz, that the second spot may be ignored. A direct comparison of the measured VLA main spot area (857.6 arcsec² in left circular polarization and 580.8 arcsec² in right circular polarization) with the area derived from the OVRO data (993 arcsec² in LH and 620 arcsec² in RH) agree to within ~15%. The validity at 1.4 GHz may also be checked by inspection of the 1.4 GHz VLA map of Figure 2.

Although this source is much larger E/W than in the N/S direction, the Moon at OVRO crosses the source at such an angle that the extents of the source along and perpendicular to the window are nearly equal. We conclude that our assumptions are valid to ~20% at 1.4 and 5 GHz, and probably no worse than ~30% at intermediate frequencies.

The brightness temperature spectrum is shown in Figure 5, separately for right and left circular polarization (5a-b) and total intensity (5c). The data are displayed as two-dimensional contour plots, with time increasing to the left on the horizontal axis, and frequency increasing downward on the vertical axis. The times along the horizontal axis correspond to the positions of the Moon shown in Figure 3. The peak brightness temperature of the main spot at 5 GHz in Figure 5 is 9×10^6 K, which is about 20% less than the 1.1×10^7 K peak brightness temperature in Figure 2. The peak brightness temperature at 1.4 GHz in Figure 5 is 1.3×10^6 K, very near the 1.33×10^6 K in Figure 2. These figures support the error estimates given in the previous paragraph.

Figure 6 shows representative spectra, corresponding to vertical cuts through Figure 5 and illustrates the quantitative effects of gyroresonance opacity and free-free emission on the spectra as a function of position. When gyroresonance opacity dominates, the spectral cutoff can be interpreted in terms of the magnetic field. Alternatively, when the fields are relatively unimportant, as in the spectrum acquired between the sunspots at 162300, the spectral shape is characteristic of free-free opacity. In this case, the coronal temperature can be directly inferred from the low frequency (optically thick) brightness temperature (1.1×10^6 K in this case). The frequency at which the emission starts becoming optically thin (3 GHz) can be interpreted in terms of the line-of-sight integral of the square of the electron density. In this case, assuming the structure is 10000 km thick, the inferred coronal density is 6×10^9 /cc.

IV. THE CORONAL PLASMA AND ACTIVE REGION STRUCTURE

A. Identification of Emission Mechanisms

Considering first the overall correspondence between the microwave data and the magnetic structure of the active region, we compare the relevant portion of a full disk magnetogram taken at Kitt Peak at 1745 UT with the VLA radio contours. The correspondence between the 4.9 GHz microwave map and the magnetogram features is very good (Figure 7). Following previous workers, we identify the emission mechanism at 4.9 GHz as gyroresonance emission, on the basis

of the following features: 1) The emission is strongly associated with the highest magnetic fields. 2) The polarization of the emission near 5 GHz in Figure 7 is predominantly left hand for spot 1 and predominantly right hand for spot 3 (the source for spot 2 is also left hand polarized in the VLA data--not shown). The sense and strength (about 50%) of polarization is as expected for gyroresonance emission, which is predominantly in the extraordinary magneto-ionic mode (x-mode). 3) The high brightness temperature emission associated with the larger spot (number 1) extends to beyond 8 GHz in the OVRO data (Figure 6), while the smaller spot (number 3) has emission extending only to about 5 GHz. This is consistent with a weaker coronal magnetic field strength overlying spot 3.

These conclusions can be strengthened by noting that the microwave spectra can be simply interpreted to indicate the strongest coronal fields associated with each spot. For example, the extension of the $6 \times 10^{15} \text{ K}$ brightness temperature of spot 3 to 5.4 GHz in Figure 5a implies a field strength of about 640 G at the height where $T \sim 6 \times 10^{15} \text{ K}$ over spot 3, assuming that the emission is optically thick at the third harmonic of the gyrofrequency (harmonic, $s = f/f_{\text{c}} = 3$).

We identify the emission mechanism in the VLA map at 1.4 GHz as free-free (bremsstrahlung) emission from the following evidence: 1) The emission is not associated especially with the highest magnetic fields. In fact, the brightest emission in Figure 7 appears to avoid the umbrae. 2) The emission extends across the active region, lying between the spots in the area commonly found in X-ray observations of other active regions to be sites of high density X-ray loops. 3) The polarization at 1.4 GHz, although uncertain, is not more than about 10%, consistent with free-free emission.

From the spectral data we can further identify that the "cross-over" point where the emission goes from predominantly one mechanism to the other occurs near 3 GHz. At frequencies higher than ~3 GHz, the spectrum shows two distinct sources corresponding to the two main spots, with quite different appearance in right and left circular polarization. At frequencies below ~3 GHz, only a single source appears, with no significant differences in the two polarizations.

B. Ring Structure and Cool Plumes

Although the features of a gyroresonance source are dominated by the magnetic field strength and structure, variations in temperature and density can play an important role as well. In Figure 7, we note that the lower contours

of the 4.9 GHz radio source associated with spot 1 are symmetric and centered on the spot. whereas the higher contours are markedly displaced toward the center of the active region. This is also true of spot 3. This is the same phenomenon as that causing the sometimes observed "ring" structure. first reported by Alissandrakis and Kundu (1982). These authors noted that the depression in brightness over the umbra might be due in part to low gyroresonance emissivity when the direction of the magnetic field makes a small angle to the line of sight. In their observations. however. the position of the ring did not vary in the expected way as the spot approached the limb, leading them to postulate the existence of cool material above the sunspot umbra. Such cool plumes have been reported from EUV observations by Foukal et al. (1974), Nicolas et al. (1982), Doyle et al. (1985), and Noyes et al. (1985). Modeling of the Alissandrakis and Kundu observations by Strong, Alissandrakis, and Kundu (1984) showed that the depression in brightness temperature could not be explained by the angular effect alone. and gave further evidence that cool material existed above the sunspot umbra.

In the present observations. the displacement of the 4.9 GHz source from the center of sunspots 1 and 3 is not due to the angular dependence of gyroresonance emissivity. If it were. the displacement would be toward the limb in both spots. whereas it is instead toward the center of the active region--toward the limb for spot 1 but away from the limb for spot 3. Another facet of the map data is that the 1.4 GHz source appears to avoid the sunspot umbrae. The spectral data (Figure 5) link these two effects by showing that the high frequency asymmetry is maintained well into the low frequency regime. to at least 1.8 GHz. where the free-free emission mechanism dominates. This is strong evidence that the asymmetry is due to a temperature and/or density deficit. and not due to gyroresonance. The sense of the asymmetry is such that there is a relative density/temperature deficit on open field lines that connect the outer areas of the umbrae. away from the center of the active region.

C. The 1.4 GHz Source: An Arcade of Loops

To gain insight into the structure of the magnetic field in the corona above the active region. a Kitt Peak magnetogram was used as the basis for a potential field calculation. using a computer program kindly provided by T. Sakurai. The program solves Laplace's equation using the spherical Schmidt method detailed by Sakurai (1985). Because the Kitt Peak magnetogram saturates at field strengths above ~1000 G, the umbral field strengths must be corrected. This was done by assuming that the sunspots could be represented by solenoids with radii equal to the spots' photospheric radii, and with central field strengths given by Zeeman

measurements from Mt. Wilson. The Mt. Wilson values, measured at 2300 UT, were -2300, -2000 and +2300 G for spots 1, 2 and 3 respectively. The implementation of the equivalent solenoid representation for sunspots is described by Sakurai and Uchida (1977). Note that the solenoid approximation merely adds the missing (saturated) magnetic flux to the magnetogram; the weaker fields are unchanged.

Although we had expected that the radio emission below 3 GHz might have come from a large-scale loop structure with field lines traversing the entire active region from east-west from spot 3 to spot 1, the results of the potential field calculation showed that this was not the case. As shown in Figure 8, the results indicate that most of the positive flux from spot 3 connects to spot 2, effectively isolating spot 1 with the field lines crossing perpendicular to the long axis of the source. Thus the enhanced density associated with the radio emission below 3 GHz is associated with an arcade of relatively low lying loops.

V. SUMMARY

The special circumstances afforded by a solar eclipse were used to obtain spatially resolved microwave brightness temperature spectra of a complex solar active region at 16 frequencies between 1.4 and 8 GHz using the Owens Valley frequency-agile interferometer. Two dimensional VLA maps at 1.4 and 4.9 GHz were also obtained, with the eclipse in this case serving to shorten the required integration time to 15 minutes and to enhance the angular resolution at the lower frequency.

At frequencies above ~3 GHz the emission was found to be primarily due to gyroresonance, and was located at sites of the strongest coronal magnetic fields. The spectral cutoff at 5.4 GHz above one spot indicates a maximum coronal field strength of about 640 G. The main spot had a stronger coronal field, >1000 G, since it remained a source of emission above 8 GHz in both polarizations.

A marked asymmetry in the position of the sources, was noted at frequencies down to at least 1.8 GHz, suggesting that a deficit of temperature and/or density existed on the field lines in the outer part of the spots, on the side away from the active region. The emission at frequencies less than 3 GHz, primarily due to thermal Bremsstrahlung (free-free) emission, did not occur at the site of strongest magnetic fields near the spots. Potential field calculations, based on a photospheric magnetogram from Kitt Peak suggest that the low frequency emission originated from the top of an arcade of loops stretching between the spots. At 1.4 GHz, the radio source appears to avoid the umbrae of the spots, perhaps in analogy with the results of Webb and

Zirin (1981) that soft X-ray sources tend to avoid spot umbrae.

In regions of low magnetic field where free-free opacity dominates even at the higher frequencies, the spectra can be interpreted in terms of coronal temperature and the line integral of density-squared. Under such circumstances, spatially resolved microwave spectroscopy can play a role similar to space-based soft X-ray images.

The qualitative interpretations presented here will be expanded in a subsequent paper in which the spatially resolved spectral information will be compared to the results of detailed numerical modeling.

ACKNOWLEDGEMENTS

We thank Dr. T. Sakurai for providing the potential field mapping software. Dr. J. Harvey for supplying the magnetogram, Dan Daugherty for his assistance with the observations and Dr. H. Zirin for helpful comments.

Additional support for analysis of Owens Valley solar data is provided by the National Science Foundation under grant ATM-8309955, which also supported the VLA data analysis. Operation of the frequency-agile interferometer is supported by the NSF under grant AST-8315217. The National Radio Astronomy Observatory is operated by Associated Universities Inc., under contract to the NSF.

REFERENCES

- Akmedov, Sh.B., Borovik, V.N., Gelfreikh, G.B., Bogod, V.M., Korzhavin, A.N., Petrov, Z.E., Diku, V.N., Lang, K.R., Willson, R.F. 1986. Astrophys. J. 301. 460.
- Alissandrakis, C.E., and Kundu, M.R. 1982, Astrophys. J. (Letters) 253. L49.
- Alissandrakis, C.E., Kundu, M.R. and Lantos, P. 1980, Astron. Astrophys. 82, 30.
- Aller, H.D., Aller, M.F., Latimer, G.E., Hodge, P.E. 1985 Astrophys. J. Suppl. 59, 513.
- Doyle, J.G., Raymond, J.C., Noyes, R.W., and Kingston, A.E. 1985, Astrophys. J. 297. 816.
- Dulk, G.A., and Gary, D.E. 1983. Astron. Astrophys. 124, 103.

- Erskine. F.T., Kundu. M.R., and Rao. A.P. 1980, Astron. Astrophys. 83. 256.
- Foukal, P.V., Huber. M.C.E., Noyes. R.W., Reeves, F., Schmahl, E.J., Timothy. J.G., Vernazza. J.E., and Withbroe. G.L. 1974, Astrophys. J. (Letters) 193. L143.
- Hurford, G.J. 1986. NASA Conf. Proc. 2421. pl91.
- Hurford, G.J. 1985, AFGL-TR-85-0092. ADA162191
- Hurford. G.J., Gary, D.E., and Garrett. H.: 1985, Radio Stars, R.M. Hjellming and D.M. Gibson. eds., (Dordrecht: Reidel), p.379.
- Hurford, G.J., Read. R.B., and Zirin, H. 1984, Solar Phys. 94, 413.
- Kundu. M.R., and Alissandrakis, C.E. 1975, Nature 257. 465.
- Kundu. M.R., Becker. R.H., and Velusamy, T. 1974, Solar Phys., 34. 185.
- Kundu. M.R., and Velusamy. T. 1980, Astrophys. J. (Letters) 240. L63.
- Lang, K.R., and Willson. R.F. 1979, Nature 278, 24.
- Lang, K.R., and Willson. R.F. 1982, Astrophys. J. (Letters) 255, L111.
- Lang, K.R., and Willson. R.F. 1983. Astron. Astrophys. 127. 135.
- Lang, K.R., Willson. R.F., and Gaizauskas V. 1983. Astrophys. J. 267. 455.
- Marsh, K.A., Hurford, G.J., and Zirin, H.: 1980. Astrophys. J. 236. 1017.
- Nicolas. K.R., Kjeldseth-Moe. O., Bartoe. J.-D.F., Brueckner. G.E. 1982, Solar Phys. 81. 253.
- Noyes. R.W., Raymond, J.C., Doyle. J.G., and Kingston. A.E. 1985, Astrophys. J., 297. 805.
- Sakurai, T.: 1985, Solar Phys. 95, 311.
- Sakurai, T., and Uchida. Y. 1977. Solar Phys. 52, 397.
- Shevgaonkar, R.K. and Kundu. M.R.: 1985, Solar Phys. 98, 119.
- Strong, K.T., Alissandrakis, C.E., and Kundu. M.R. 1984, Astrophys. J. 277. 865.

Webb, D.F. and Zirin, H.: 1981. Solar Phys. 69, 99.

FIGURE CAPTIONS

Figure 1. The geometry of the eclipse as seen from the VLA. The area within the square box was mapped at 1.45 and 4.9 GHz from 1635 to 1650 UT. during which time the lunar limb moved as shown by the labeled arcs. Boulder Region 4500 is at the center of the mapped area.

Figure 2. The eclipse maps obtained at the VLA at 4.9 (left) and 1.45 (right) GHz. The contours in the 4.9 GHz map are every 10% of the peak $T_{\text{dn|b|up}} = 1.10 \times 10^6 \text{ |dn| K}$. The contours at 1.45 GHz are every 20% of the peak $T_{\text{dn|b|up}} = 1.33 \times 10^6 \text{ |dn| K}$. The positions of the centers of the three sunspots, as measured from optical full disk images, are as shown. The spot positions were measured with greater accuracy than is typically possible by utilizing the sharply defined lunar limb that was visible in the optical images.

Figure 3. The position of the lunar limb at one minute intervals as seen from OVRO is shown superimposed on the 4.9 GHz map. Since the time resolution of the OVRO spectra was 10 s, six independent 16-frequency spectra were obtained within each of the one minute intervals shown.

Figure 4. Differenced OVRO time profiles at four representative frequencies. Right hand circular (RH) polarization is shown by the heavy lines, and left hand (LH) polarization by the light lines. Below ~3 GHz, the active region appears as a single broad source. At higher frequencies, the region bifurcates into two main sources, becoming more localized to the sunspots as the observing frequency increases. The difference sense of polarization in the two spot sources is characteristic of gyroresonance emission.

Figure 5. The OVRO "spatial dynamic spectrum" displaying contours of brightness temperature as a function of time and frequency in a) right hand circular polarization, b) left hand circular polarization, and c) total intensity. The times during which the OVRO window overlies a sunspot umbra are indicated below the time axes. The brightness temperature contours are 1.2, 1.0, 0.8, 0.6, 0.4, and $0.2 \times 10^6 \text{ |dn| K}$. The time axis is shown increasing to the left because the lunar limb was moving right to left.

Figure 6. Representative difference spectra corresponding to different 2.6 arcsecond wide annuli. The times indicated in each panel may be used to identify the location of each spectrum by reference to Figure 3. At 161640, the polarization and sharp cutoff in the spectrum is characteristic of gyroresonance opacity with a maximum upward-directed field strength of about 500 gauss. The field strength increases until by 161840, when the annulus crosses the main spot. the cutoff is above the maximum observing frequency of 8 GHz. At 1620, the spectrum suggests gyroresonance opacity operative in the quasi-transverse approximation. where the polarization is relatively low. At 1623, the spectrum of an annulus that is between the spots is characteristic of free-free emission. That is the optically thick brightness temperature is flat at low frequencies and when it becomes optically thin at higher frequencies. it follows an inverse square law. By 162410, gyroresonance opacity from the downward-directed fields from the other sunspot dominates. Note the different sense of polarization compared to the other spot.

Figure 7. The 4.9 and 1.45 GHz VLA eclipse maps overlaid on magnetograms obtained at Kitt Peak. Note the excellent correspondence with high field regions at 4.9 GHz, and the poor correspondence at 1.45 GHz. The 4.9 GHz sources are due to gyroresonance emission and the 1.45 GHz source is due to free-free emission.

Figure 8. A plot of magnetic field lines in the active region. based on a potential field model extrapolation to coronal heights. The field lines are seen projected onto contours of the longitudinal photospheric field measured at Kitt Peak. The 1.45 GHz radio source lies along the "arcade" of loops extending southward from the two negative polarity spots (dashed contours) and also connecting the opposite polarity following spots.

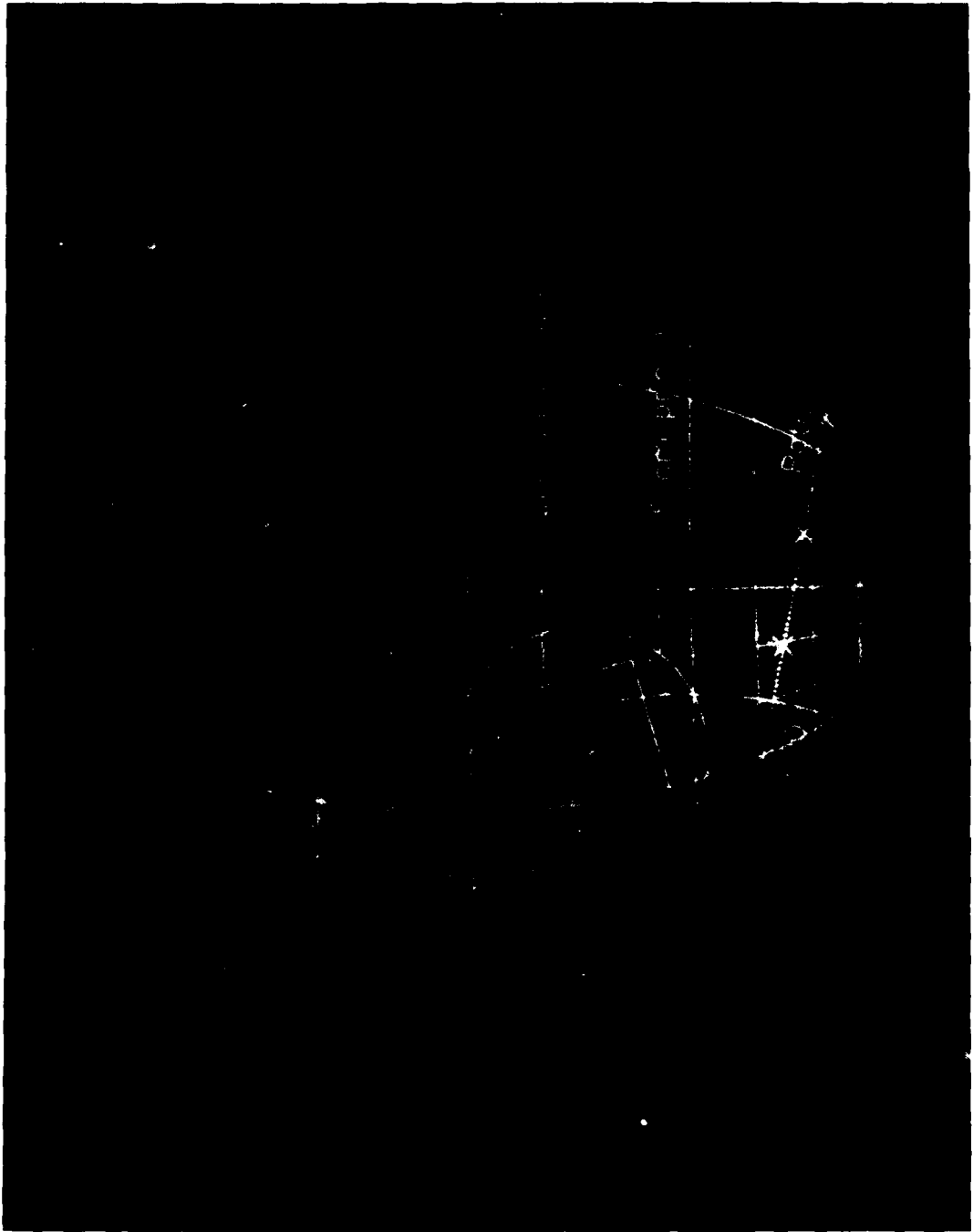


Figure 1

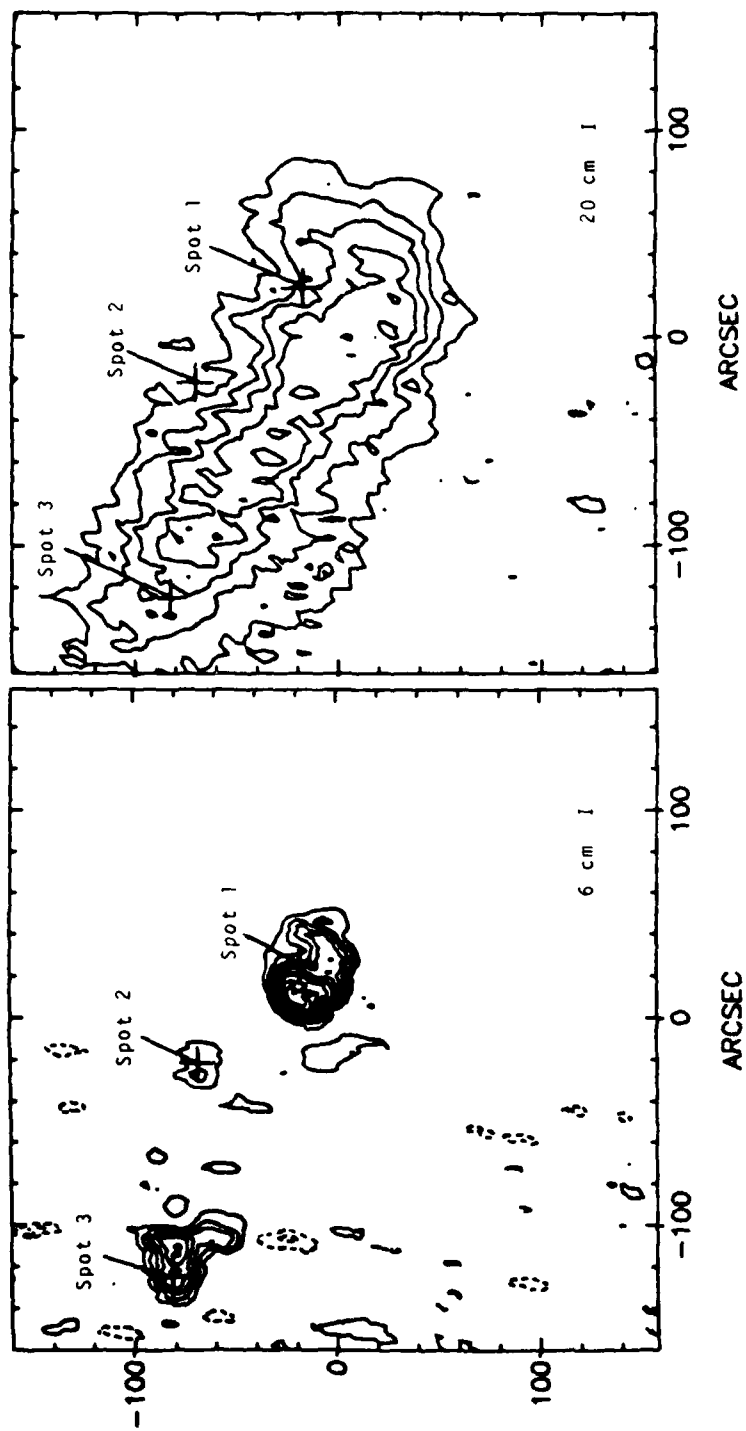


Figure 2

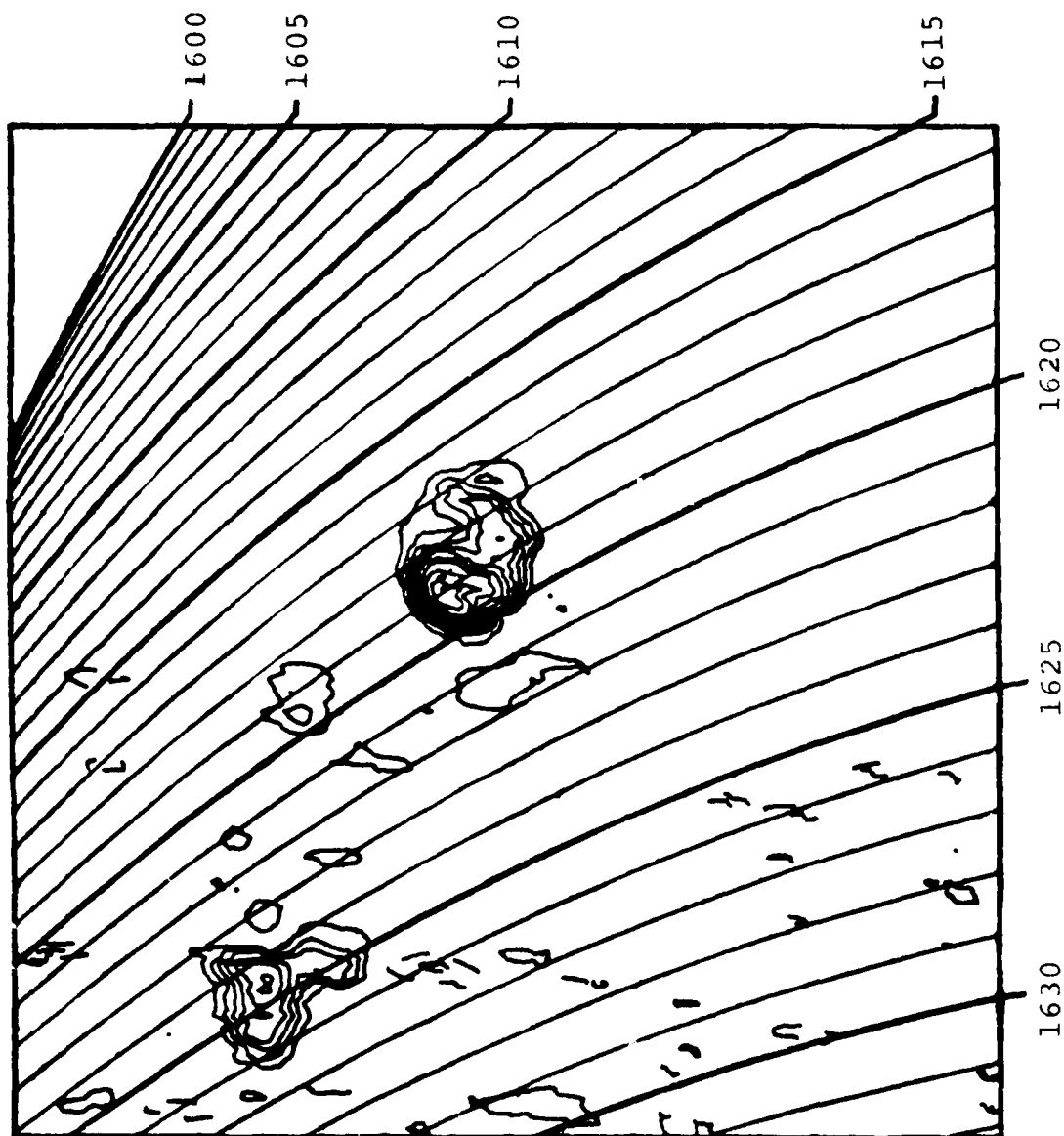


Figure 3

REPRESENTATIVE DIFFERENCE PROFILES

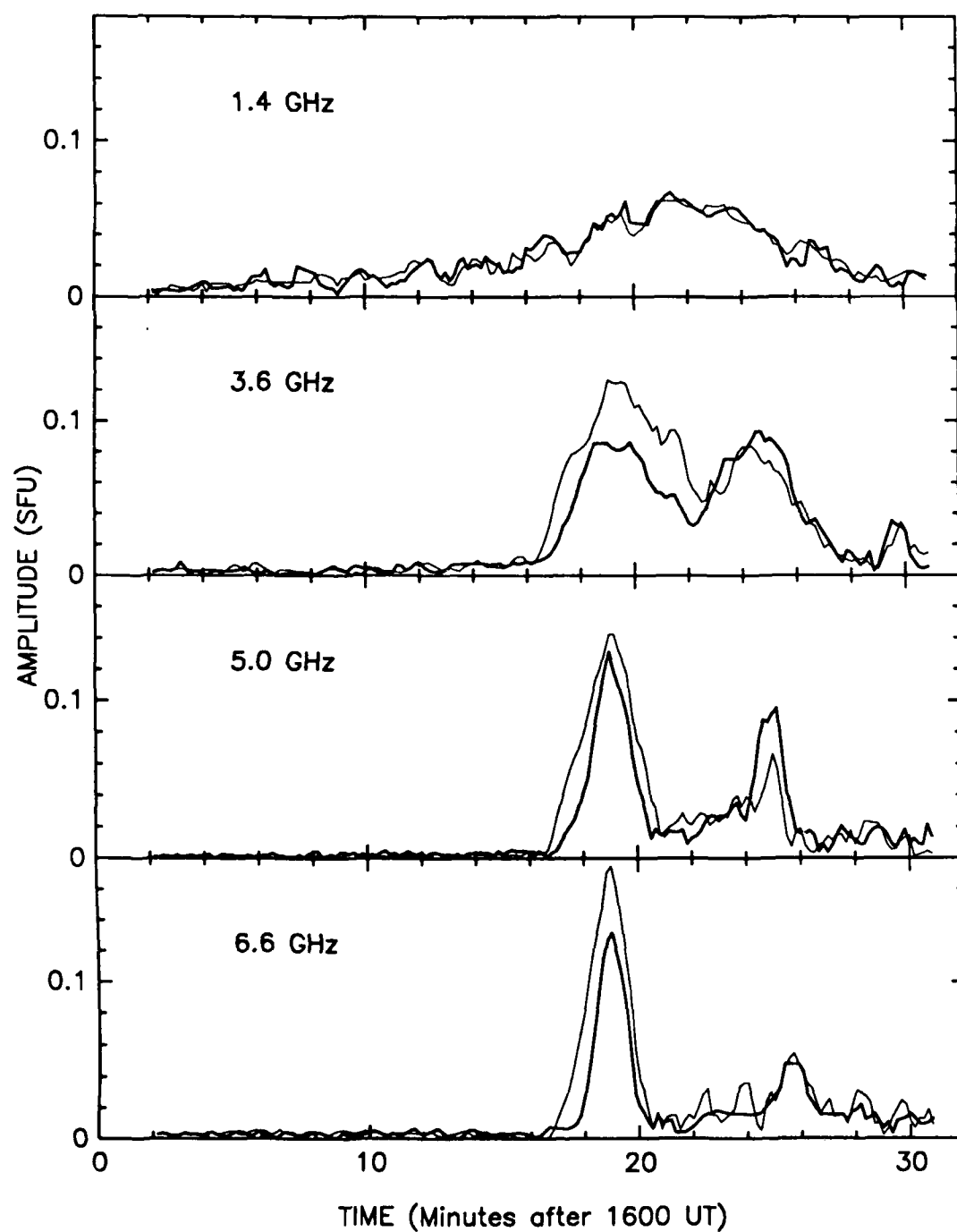


Figure 4

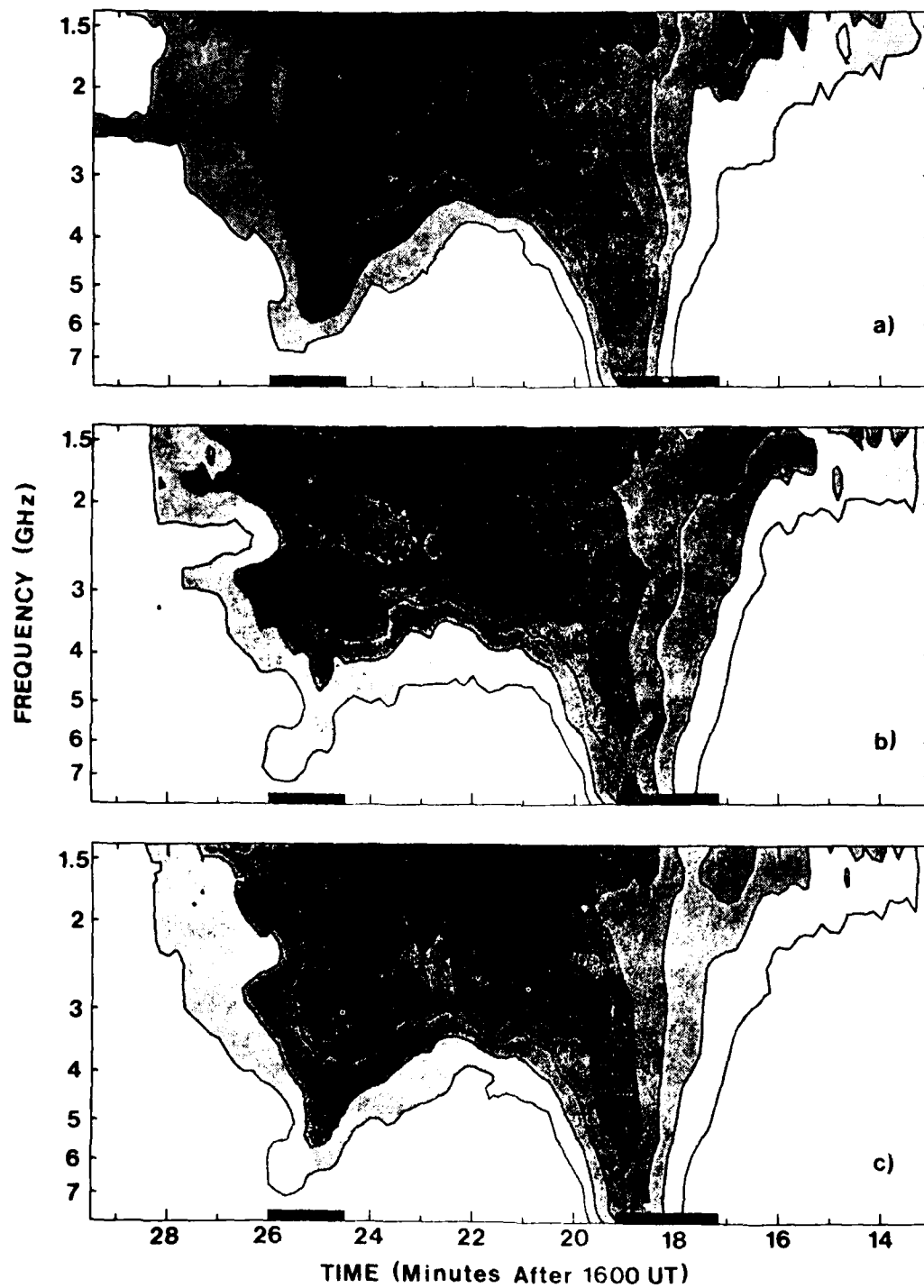


Figure 5

REPRESENTATIVE DIFFERENCE SPECTRA

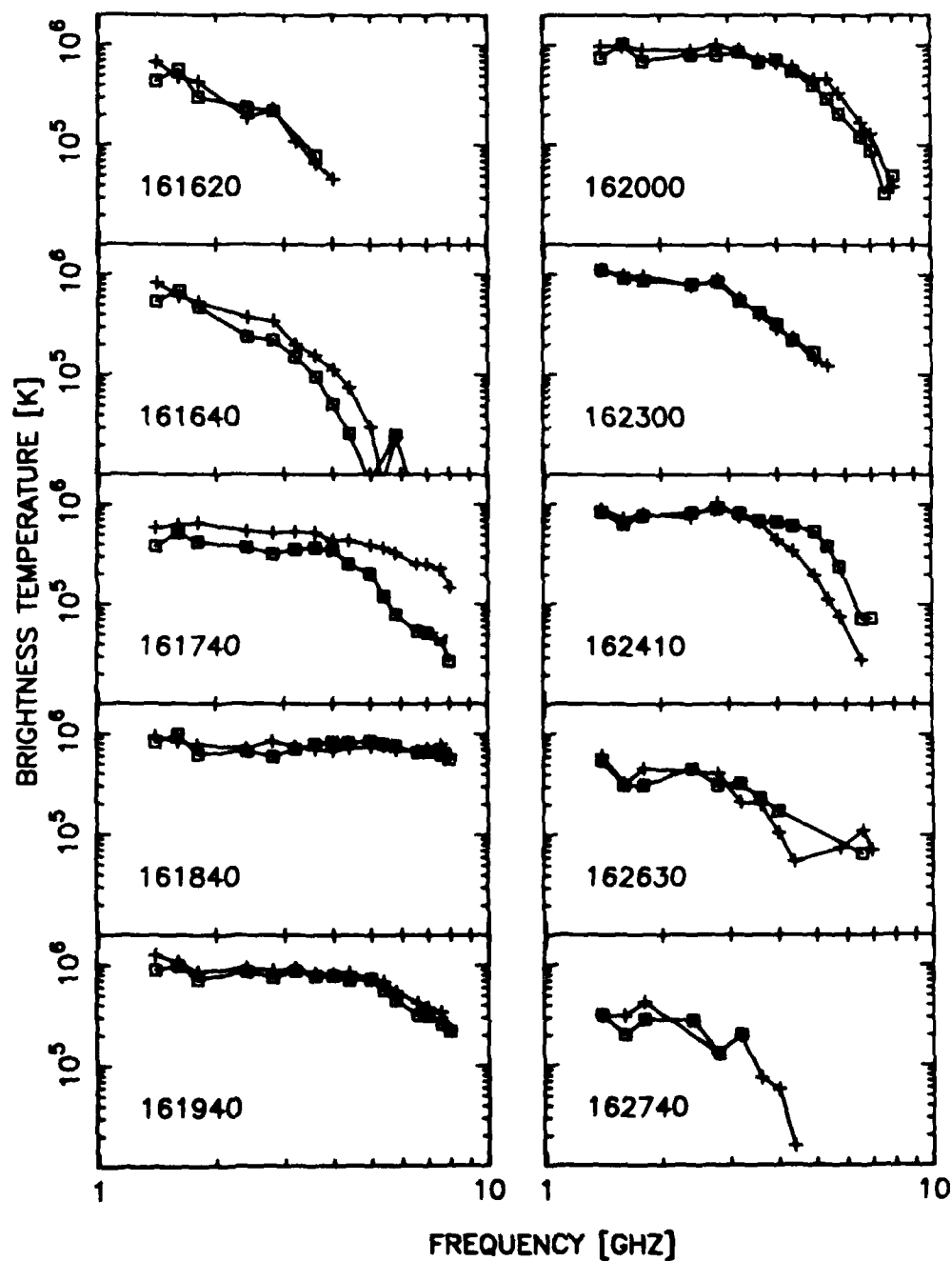


Figure 6



Figure 7

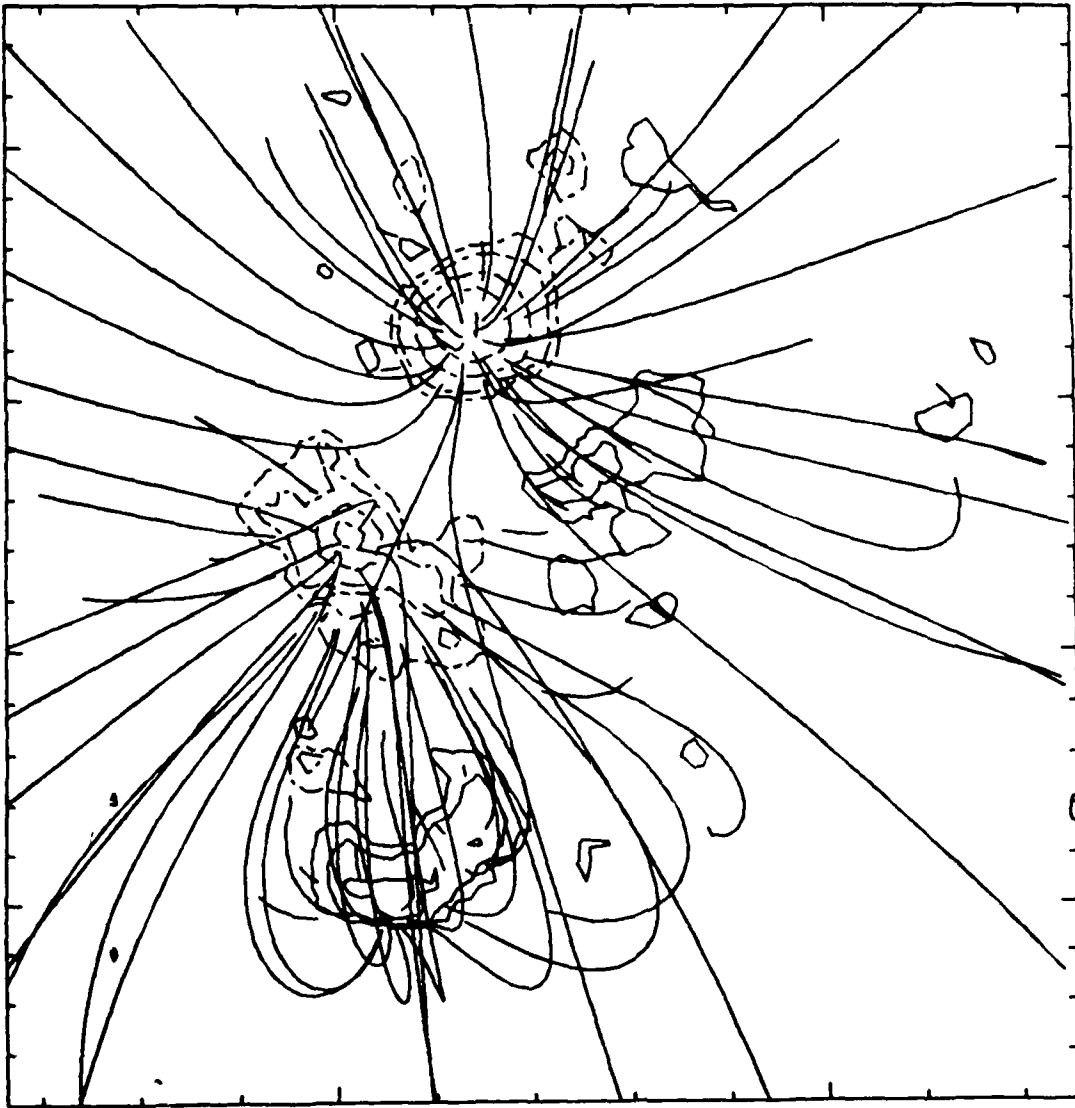


Figure 8

DATE
FILMED
- 8